



On the pitting corrosion of 2205 duplex stainless steel produced by laser powder bed fusion additive manufacturing in the as-built and post-processed conditions

Nima Haghdadi ^{a,*}, Majid Laleh ^{b,c}, Hansheng Chen ^d, Zibin Chen ^{d,e}, Carina Ledermueller ^a, Xiaozhou Liao ^d, Simon Ringer ^d, Sophie Primig ^{a,*}

^a School of Materials Science & Engineering, UNSW Sydney, NSW 2052, Australia

^b School of Engineering, Deakin University, Waurn Ponds, VIC 3216, Australia

^c Institute for Frontier Materials, Deakin University, Waurn Ponds, VIC 3216, Australia

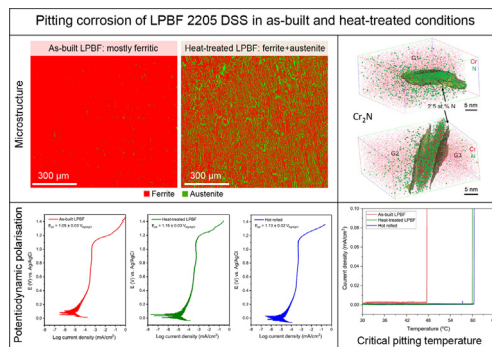
^d Australian Centre for Microscopy & Microanalysis, and School of Aerospace, Mechanical and Mechatronic Engineering, The University of Sydney, NSW 2006, Australia

^e Department of Industrial and Systems Engineering, The Hong Kong polytechnic University, Hong Kong, China

HIGHLIGHTS

- 2205 DSS shows similar pitting potentials and passive current densities at RT irrespective of processing route.
- Cr is depleted adjacent to intergranular Cr₂N particles but remains above the critical value for passivation.
- As-built LPBF 2205 DSS shows a lower CPT compared to its hot-rolled counterpart.
- Post-AM heat treatment enhances the critical pitting temperature to the level of the hot-rolled DSS.

GRAPHICAL ABSTRACT



ARTICLE INFO

Article history:

Received 3 August 2021

Revised 14 November 2021

Accepted 17 November 2021

Available online 18 November 2021

Keywords:

Additive manufacturing

Duplex stainless steel

Microstructure

Pitting corrosion

Heat treatment

ABSTRACT

The effects of additive manufacturing (AM) and post-AM heat treatment on microstructural characteristics and pitting corrosion of 2205 duplex stainless steel were studied and benchmarked against its conventionally hot-rolled counterpart. The rapid solidification and possible loss of N associated with AM resulted in a non-equilibrium microstructure dominated by δ-ferrite with a minor fraction of austenite and abundant Cr₂N precipitation. Atom probe tomography revealed that no depletion of Cr occurs around intragranular Cr₂N. A deduction in Cr was observed adjacent to intergranular Cr₂N particles, however, Cr content in these regions remained above the critical value of 13 wt%. Post-AM heat treatment was effective in restoring the duplex microstructure while dissolving the Cr₂N precipitates. Although the pitting resistance in the as-built AM specimen was lower than that of its hot-rolled counterpart, it was fully recovered after post-AM heat treatment.

© 2021 The Author(s). Published by Elsevier Ltd. This is an open access article under the CC BY-NC-ND license (<http://creativecommons.org/licenses/by-nc-nd/4.0/>).

1. Introduction

Following the great progress in additive manufacturing (AM) during the past decades, many industry sectors now attempt to use this technology to enable the production of complex 3D

* Corresponding authors.

E-mail addresses: nima.haghdadi@unsw.edu.au (N. Haghdadi), s.primig@unsw.edu.au (S. Primig).

geometries in a single step while reducing lead time and cost [1,2]. Apart from design flexibility, AM has also unlocked new combinations of attractive material properties [3] such as mechanical [4–6] and corrosion [7–9] properties that are often not attainable through conventional manufacturing routes. These improvements can be related to the unique microstructural features in AM materials resulting from complex thermal histories (e.g., rapid cooling and cyclic reheating) during AM processing. These features include the grain morphology [10,11], grain boundary characteristics [12], local chemical compositions [13], and morphology of precipitates/inclusions [14,15], to name just a few. All these features would influence the properties of AM materials in comparison to what is expected for their conventionally manufactured counterparts. Such differences between AM and conventionally manufactured materials necessitates thorough investigations and benchmarking of microstructure–property relationships.

Among various groups of metallic materials currently processed by AM, stainless steels have gained considerable attention due to their widespread applications in several industries, including biomedical, petrochemical, marine, oil & gas, and construction [16]. The majority of the available literature on AM stainless steels has focussed on austenitic and precipitation-hardening stainless steels, whose processing–microstructure–property relationships have been studied in several research and review papers, for instance in references [17,18]. However, duplex stainless steels (DSSs), as a group of important engineering materials especially suitable for applications such as pressure vessels, heat exchangers, and underwater infrastructure, have so far received less attention in the AM literature, particularly in terms of their corrosion behaviour. This could be partially related to the challenges associated with achieving a balanced duplex microstructure of roughly equal fractions of austenite and δ-ferrite similar to that obtained in conventional manufacturing [3,19].

DSSs are usually characterised by their balanced δ-ferrite/austenite microstructures, offering an excellent combination of corrosion resistance and mechanical properties, with both higher strength and toughness due to the presence of two equilibrium phases. However, previous studies have found that δ-ferrite (referred to as ferrite in the following) is the major phase in laser powder bed fusion (LPBF) duplex stainless steels in the as-built state [20–23]. This has been attributed to the high cooling rates inherent to LPBF processing which favour the formation of a dominantly ferritic microstructure via largely bypassing the austenite transformation nose. Typical austenite contents reported in the as-built condition of LPBF DSSs are less than 5%. However, a balanced microstructure could be restored (back to > 40% austenite) via an appropriate post-AM heat treatment [21,23,24]. This post-processing heat treatment is therefore essential to restore the equilibrium duplex microstructure and mechanical properties of DSSs. In conventional manufacturing, post-fabrication annealing has commonly been applied to modify the microstructure, control the proportion of ferrite and austenite phases, redistribute alloying elements, and change the grain morphology with the aim of enhancing both the mechanical and corrosion properties of DSSs [25–27].

While there are some studies on the mechanical properties of AM DSSs in both as-built and post-AM heat treated conditions, the corrosion behaviour has received less attention so far, and results are ambiguous to some extent. Murkute et al. [28] reported a decrease in corrosion rate with an increased amount of austenite in heat-treated AM 2507 super duplex stainless steel, showing an indirect evidence of the positive influence of austenite on corrosion performance. In contrast, Jiang et al. [29] reported similar pitting and re-passivation potentials for as-built LPBF 2205 duplex and 2507 super duplex stainless steels compared to their heat-treated and conventional counterparts in sodium chloride solution at room

temperature. Nevertheless, the processing–microstructure–corrosion relationships in LPBF DSSs are yet to be investigated in detail, especially at temperatures above room temperature, and after post-AM heat treatments. Critical pitting temperature (CPT) experiments have commonly been used as a criterion for determining the pitting susceptibility of conventional DSSs versus temperature [30,31], but this technique has not yet been applied to study AM DSSs.

The current study aims to fill these important knowledge gaps in understanding the pitting corrosion behaviour of DSSs. DSS 2205 samples were produced by LPBF and subsequently annealed. Polarisation measurements and CPT experiments were employed to investigate the pitting corrosion resistance in both as-built and heat-treated conditions. The corrosion behaviour of a benchmark hot-rolled DSS 2205 specimen was also investigated for comparison purposes. A range of microscopy analyses techniques from micron to atomic scale were carried out to understand the influence of microstructural characteristics on pitting corrosion.

2. Materials and methods

2.1. Materials

Gas atomised spherical powder particles of 2205 DSS (purchased from Sandvik Osprey Ltd) with a size range of ~ 15 – 53 µm (measured via Sieve and lase diffraction analysis) were used. The chemical composition of the powder was 0.02C, 22.60 Cr, 5.90 Ni, 1.10 Mn, 3.20 Mo, 0.02P, 0.6Si, 0.18 N, 0.01 S, and the balance Fe (in wt%). LPBF processing was performed using an SLM Solution 125^{HL} machine with a 400 W laser purged with Ar, and the processing parameters given in Table 1. These parameters are the optimised parameters to achieve a high density and avoid the formation of lack-of-fusion (LOF) pores. Cubes with an edge length of 15 mm were printed. The relative density of the as-built LPBF specimen was measured to be ~ 99.6%, according to the Archimedes principles using an Electronic Densimeter (Model SD-200L) with a 0.1 mg/cm³ resolution. Before density measurements, the specimen was ultrasonically cleaned in ethanol for 10 min to remove the residual powder attached to the surface from the LPBF processing.

Half of the as-built LPBF specimens were subjected to post-AM heat treatment at the temperature of 1000 °C for 10 min followed by water quenching to room temperature. The temperature for annealing was selected based on the previous studies on the same steel to maximise austenite fraction [21] while avoiding formation of undesired Sigma phase [32]. For benchmarking purposes, a hot-rolled 2205 DSS with the chemical composition of 0.036 C, 0.321Si, 1.82 Mn, 0.013 P, 23.2 Cr, 5.6 Ni, 2.90 Mo, 0.034 Co, 0.153 Cu, 0.245 N and the balance Fe (in wt%) received in the form of a plate with a thickness of 20 mm was also subjected to the same corrosion investigations.

2.2. Microstructural analysis

Electron backscatter diffraction (EBSD) was carried out using a JEOL 7001F scanning electron microscope (SEM) equipped with a Hikari 31 Super EBSD Camera. The parameters for the EBSD scans were an acceleration voltage of 25 kV, a probe current of 14nA, 6 × 6 binning, and a step size of 1 µm. The TSL-OIM software was used for data collection and analysis.

Transmission electron microscopy (TEM) characterisation was conducted on thin foils prepared via a standard electropolishing procedure. A Themis-Z double-corrected microscope working at 300 kV was used for TEM analysis. Samples were studied using a combination of bright-field TEM imaging and low angle annular

Table 1

The LPBF processing parameters for producing DSSs used in this study.

Laser power	Scan speed	Hatch spacing	Layer thickness	Rotation between layers
200 W	700 mm s ⁻¹	60 µm	30 µm	67 deg

dark field (LAADF) scanning transmission electron microscopy (STEM) imaging.

Atom probe tomography (APT) tips were prepared either by a standard electropolishing or focussed ion beam (FIB)-assisted lift-out techniques. For the electropolishing, samples were first sectioned into blanks of $\sim 0.5 \times 0.5 \times 10 - 15$ mm³, followed by rough-polishing in a 25% perchloric acid at room temperature at a voltage of ~ 20 V. They were then annular milled using either a Xe plasma (ThermoFisher G4) or a Ga FIB-SEM (Zeiss Auriga) at 30 kV. As the last step, all tips were annularly milled with lower voltages to remove the damaged surface layers. The Xe plasma FIB-SEM was used for site-specific preparation of an APT tip containing a ferrite-ferrite grain boundary following the procedures described in [33]. A CAMECA 4000X Si local electrode atom probe (LEAP) equipped with a picosecond-pulse ultraviolet laser ($\lambda = 35$ 5 nm, laser frequency = 200 kHz, laser pulse energy = 50 pJ) was used for the APT analysis. The base temperature was maintained at ~ 50 K. Cameca's Integrated Visualization & Analysis Software (IVAS) version 3.8.4 [34] was used for APT data reconstruction.

2.3. Electrochemical experiments

For electrochemical experiments, specimens with a surface area of 1 cm² were connected to copper wires from their backsides to create an electrical connection, and then embedded in an epoxy resin with the transverse plane (perpendicular to the building direction) as the testing surface. Prior to electrochemical measurements, specimens were mechanically ground with SiC papers down to 4000 grit, degreased with ethanol, rinsed with distilled water, and dried in hot air. All electrochemical measurements were conducted in 1.0 M NaCl solution in a glassy three-electrode cell consisting of Ag/AgCl electrode as the reference electrode, a Pt-coated Ti mesh as the counter electrode, and the testing specimen as the working electrode, using a VMP3 potentiostat (Bio-Logic Science Instruments). All electrochemical measurements were repeated at least five times, and average values with their standard deviations were reported.

Potentiodynamic polarisation measurements were carried out by sweeping the potential from -0.2 V below open circuit potential (OCP) to $+1.4$ V above OCP with a scan rate of 10 mV/min at a controlled room temperature (22 ± 2 °C). The tests were set to be stopped when the current density reached $100 \mu\text{A}/\text{cm}^2$. Prior to polarisation tests, the specimens were immersed into the test solution for 30 min in order to obtain a stable potential.

CPT experiments were conducted based on the ASTM G-150-13 method. For CPT measurements, an anodic potential of 750 mV vs. Ag/AgCl was applied while the solution temperature was increased at a constant rate of ~ 1 °C/min. The current density was continuously recorded at the frequency of 0.01 with temperature changes until the current density increased to $100 \mu\text{A}/\text{cm}^2$ and was steady above it, according to ASTM G-150-13. The temperature at which the current density equals to $100 \mu\text{A}/\text{cm}^2$ is reported as CPT.

3. Results and discussion

3.1. Microstructure and phase analysis

The EBSD phase map of the as-built LPBF specimen (Fig. 1a) shows a predominantly ferritic structure with a small fraction

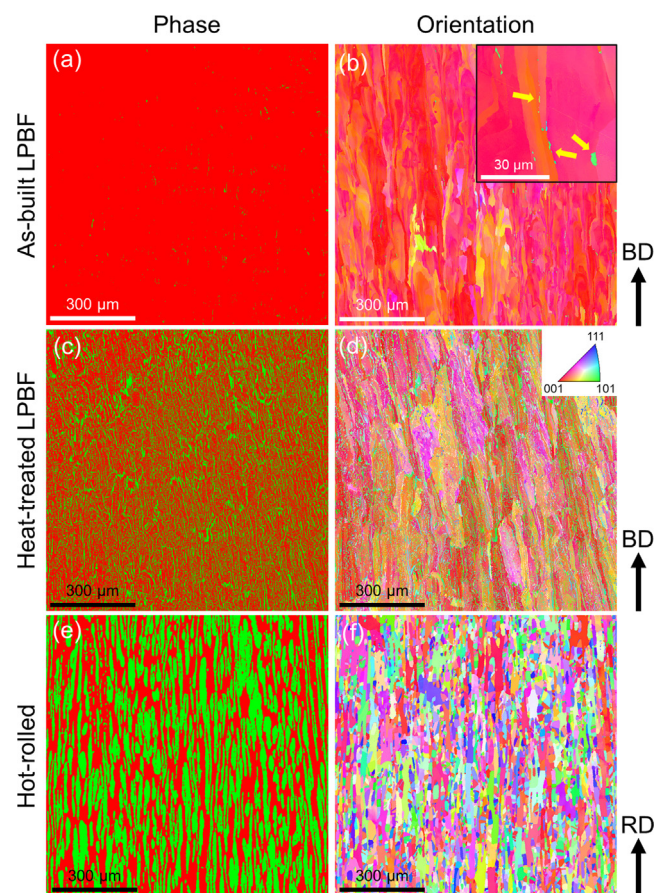


Fig. 1. EBSD phase maps (left column) and orientation maps (right column) of (a, b) as-built LPBF, (c, d) heat-treated LPBF, and (e, f) hot-rolled 2205 DSS specimens. In the phase maps, red is ferrite and green is austenite. The inverse pole figure (IPF) colour code of maps in b, d and e is with regards to the build direction in the AM and rolling direction in the hot-rolled samples. The black arrow on the right shows the build/rolling direction (BD/RD). The inset in (b) is a higher magnification IPF map of the same microstructure with yellow arrows showing examples of intergranular austenite particles. (For interpretation of the references to colour in this figure legend, the reader is referred to the web version of this article.)

($\sim 2\%$) of austenite phase at the grain boundaries (see yellow arrows in the inset of Fig. 1b). The austenite particles are in the shape of thin layers and are mostly spread along the ferrite/ferrite grain boundaries. Ferrite grains also show internal misorientation gradients, manifested by small changes in the inverse pole figure (IPF) colouring within ferrite grains. Such gradients are usually introduced as a result of solidification to accommodate strain gradients across a grain. The IPF map of the as-built specimen (Fig. 1b) shows ferrite grains with strong $\langle 001 \rangle$ orientation parallel to the build direction (BD), which resulted from the directional thermal gradients during the LPBF processing. Post-AM heat treatment is shown to promote austenite formation both intergranularly and intragranularly (Fig. 1c). During post-AM heat treatment, the austenite content increases to $\sim 45\%$. Intragranular austenite particles have an average size of 2 µm. Interestingly, ferrite preserves its $\langle 100 \rangle/\text{BD}$ texture (Fig. 1d). This is indicative of a phase transformation from ferrite to austenite towards the equilibrium phase

balance and static recovery of dislocations within ferrite. The hot-rolled sample shows a typical pancaked grain structure with a phase balance of about ~ 48% austenite and 52% ferrite. The average grain size for ferrite and austenite in the hot-rolled sample are 65 and 35 μm , respectively (Fig. 1e,f).

Based on the Cr/Ni equivalent versus temperature phase diagram (Fig. 2) of steels [35], DSSs with a $\text{Cr}_{\text{eq}}/\text{Ni}_{\text{eq}}$ ratio above 1.95 solidify as 100% ferrite above the ferrite solvus line. Below this line, the ferrite to austenite transformation begins, whose nature depends on the chemical composition, ferrite grain size, and the cooling rate [36,37]. Under extremely rapid cooling conditions as observed during LPBF processing, the ferrite content in the solidified material remains high since the time required for ferrite to austenite transformation is insufficient [38]. Another factor that might affect the austenite fraction is the loss of the austenite stabiliser N during LPBF processing. It has been reported that during welding, the extremely high temperatures in the arc combined with pure argon as shielding gas may cause a loss of N from the melt pool [39]. A reduction in N content, in turn, is expected to lower the austenite content [40]. Upon post-AM heat treatment, alloying elements will readily diffuse. As a result, the transformation of ferrite to austenite (which was suppressed due to the fast cooling associated with LPBF processing) will take place quickly, resulting in further growth of existing austenite (mostly as austenite allotriomorphs), and parallel nucleation of new austenite grains on sub-grain boundaries, dislocations and nano-scale precipitates/particles.

The bright-field TEM image of the as-built LPBF specimen (Fig. 3a) shows a high density of dislocations, which is believed to be induced due to the high solidification rates and thermal stresses associated with LPBF processing [21]. A large number of small rod-shaped particles are observed to be precipitated in the as-built LPBF specimen within the ferrite grains, as depicted in the higher magnification STEM image in Fig. 3b. The associated EDS analysis in Fig. 3b reveals the enrichment of Cr and N in these secondary precipitates, indicating the formation of Cr-rich nitrides, identified as Cr_2N . Most of these Cr_2N particles are precipitated intragranularly inside the ferrite grains (see yellow arrows in Fig. 3b,c). In addition, some intergranular Cr_2N can be observed along the ferrite grain boundaries, as shown in the STEM image in Fig. 3c (see blue arrows). The fast cooling inherent to LPBF results in a non-equilibrium ferritic microstructure supersaturated with N. Since

the solubility of N in ferrite diminishes significantly with lowering the temperature and N has a relatively high diffusivity in ferrite enriched with dislocations, the excess N precipitates in the form of Cr_2N particles. The microstructure also contains oxide inclusions typical of LPBF stainless steels (see red arrows in Fig. 3b,c).

The majority of Cr_2N particles easily dissolve at 1000 °C, as after the short-time heat treatment in this study, no Cr_2N precipitates can be detected in the heat-treated LPBF specimen (Fig. 4). The STEM/EDS analysis in Fig. 4b also shows the expected partitioning of alloying elements between ferrite and austenite phases, where Cr and Mo are concentrated in ferrite and Ni in austenite.

3.2. Corrosion behaviour

Fig. 5 shows representative potentiodynamic polarisation curves for different specimens recorded in 1.0 M NaCl solution at 22 ± 2 °C. All specimens exhibit a wide passive range and a passive current density of less than $1 \mu\text{A}/\text{cm}^2$, indicating the formation of a protective passive film on the surface. This film inhibits the materials from being corroded at high anodic potentials. At anodic potentials higher than $1 \text{ V}_{\text{Ag}/\text{AgCl}}$, the current density started to increase due to the breakdown of the passive film. The breakdown/pitting potentials acquired from these curves along with their standard deviations are presented in Fig. 5 for each specimen. As can be seen, the hot-rolled specimen exhibits the highest pitting potential of ~ 1.13 $\text{V}_{\text{Ag}/\text{AgCl}}$. The as-built LPBF specimen shows a lower pitting potential (~ 1.05 $\text{V}_{\text{Ag}/\text{AgCl}}$) compared to the hot-rolled one, despite its ferritic microstructure with abundant Cr_2N precipitates. Fig. 5 also shows that the heat-treated LPBF specimen has a pitting potential comparable to its hot-rolled counterpart (1.15 vs. 1.13 $\text{V}_{\text{Ag}/\text{AgCl}}$) and slightly higher than in the as-built LPBF specimen (1.15 vs. 1.05 $\text{V}_{\text{Ag}/\text{AgCl}}$). Therefore, the polarisation measurements at room temperature do not show any significant difference in pitting corrosion resistance between the as-built and heat-treated LPBF 2205 DSS and their hot-rolled counterpart. Indeed, the finely dispersed Cr_2N precipitates seem to not act as localised corrosion initiation sites at the testing conditions in this study, which is in excellent agreement with the findings of Bettini et al. [42] for the same grade of DSS in a similar solution. For the welded joints of DSSs and those exposed to post-manufacturing heat treatments at high temperatures (usually above 1100 °C) where many Cr_2N precipitates are formed upon cooling, it is generally known that the Cr-depleted regions around the Cr_2N precipitates act as the corrosion initiation sites when exposed to aggressive environments. However, the susceptibility of Cr_2N precipitates to localised corrosion initiation depends on their size, distribution and local chemical environment.

To study the influence of Cr_2N on pitting corrosion in more detail, APT was carried out. Two different types of Cr/N rich regions (i.e., intragranular and intergranular) showed different chemistry and depletion behaviour. Fig. 6 shows the results of the APT analysis with ferrite/Cr₂N interfaces highlighted by 2.5 at.% N iso-concentration surfaces. Fig. 6a shows an intragranular Cr-N rich region (Cr_2N) with curved interfaces in the ferrite grain. Fig. 6c shows a 5-nm wide intergranular Cr-N rich region with flat interfaces between the ferrite grains #2 (G2) and #3 (G3). A decrease in Cr content was observed adjacent to the Cr/N-rich intergranular region (Cr_2N), while no such trend was detected for the intragranular one. Despite this reduction in Cr, the minimum Cr content was recorded to be 15.3 at.% (14.6 wt%). This means that no depletion of Cr to critical values below 13% (passivity level for stainless steels [43]) occurs at regions adjacent to the Cr_2N precipitates, as shown in Fig. 6, which might be an explanation for why the pitting potential in the as-built LPBF specimen was not deteriorated compared to its hot-rolled counterpart despite the presence of Cr_2N precipitates.

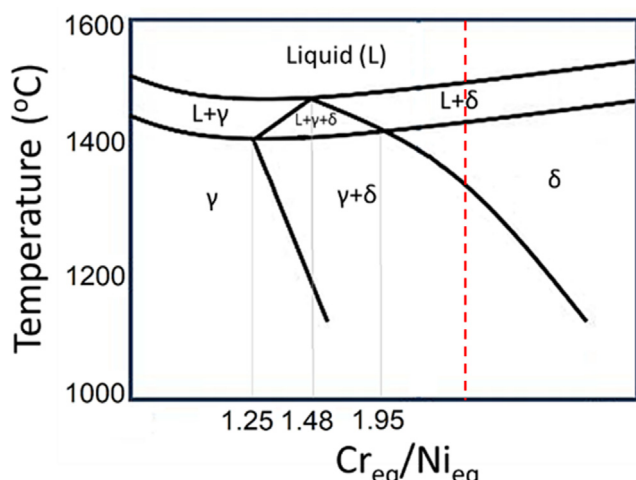


Fig. 2. The phase diagram of steels based on $\text{Cr}_{\text{eq}}/\text{Ni}_{\text{eq}}$ ratio. Replotted after [35]. The $\text{Cr}_{\text{eq}}/\text{Ni}_{\text{eq}}$ (based on the definition given in Reference [41]) for the steel under study is defined by the red dashed line. (For interpretation of the references to colour in this figure legend, the reader is referred to the web version of this article.)

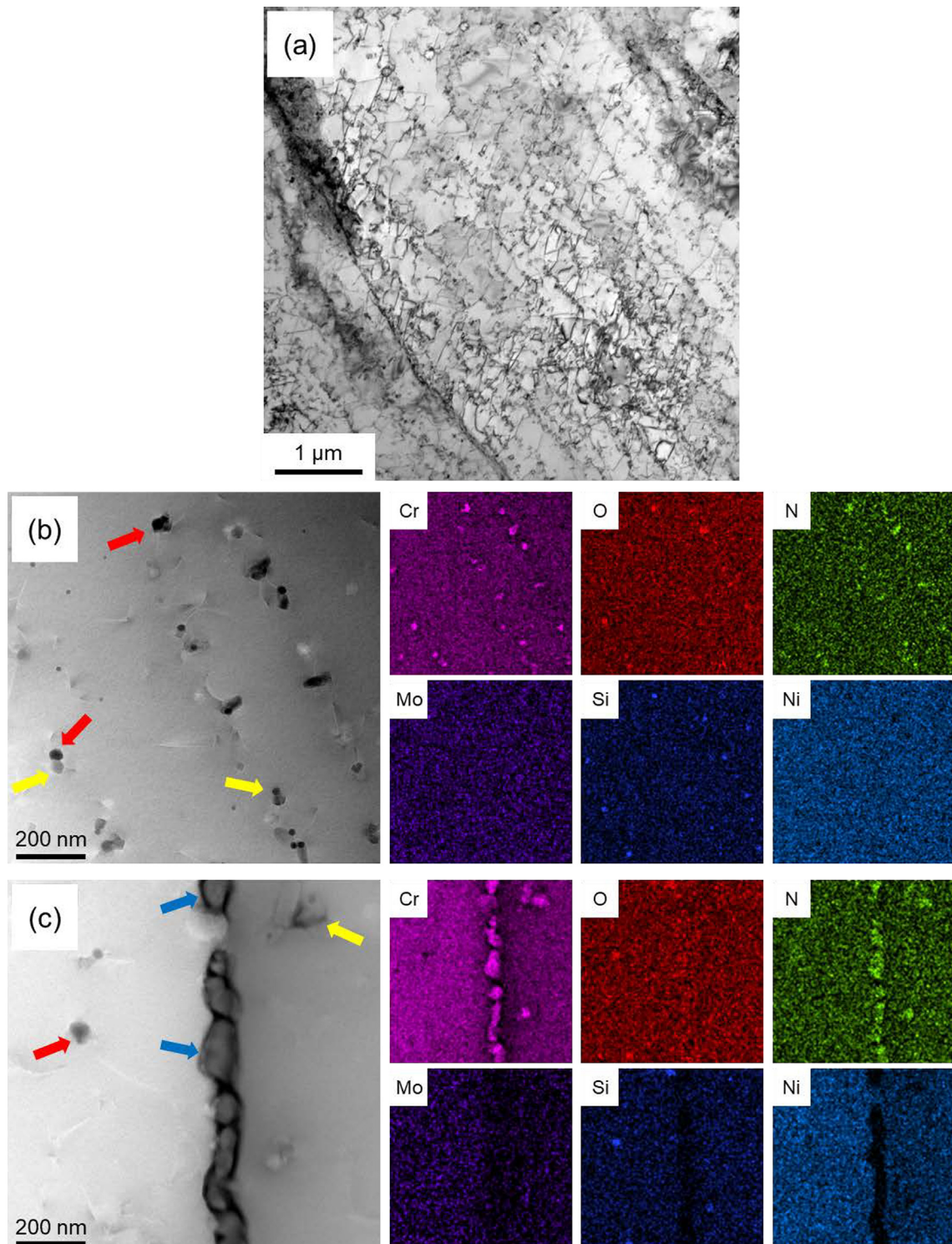


Fig. 3. (a) Bright-field TEM images showing the ferrite grain morphology and defects inside a grain in the as-built LPBF sample. (b and c) LAADF-STEM images of intragranular and intergranular regions of the microstructure, respectively, and corresponding elemental information showing segregation of alloying elements in different phases inside and at the boundaries of ferrite grains. Yellow and blue arrows show examples of intragranular and intergranular Cr_2N , respectively, while red arrows point out some of the oxide inclusions typical of LPBF stainless steels. (For interpretation of the references to colour in this figure legend, the reader is referred to the web version of this article.)

For DSSs, critical pitting temperature (CPT) is an important criterion for classifying the pitting corrosion resistance above room temperature. Fig. 7 shows representative curves of current density changes versus temperature for different specimens. At the beginning of the test, the current density decreases sharply until reaching a constant value below $1 \mu\text{A}/\text{cm}^2$, indicating the formation of a

stable passive film on the surface. By raising the temperature, the current density becomes stable although some current fluctuations appear, which implies metastable pitting (i.e., passive film dissolution and re-formation). This is followed by a sharp increase in current density which is an indication for stable pit formation. The temperature at which the current density passes $100 \mu\text{A}/\text{cm}^2$ and

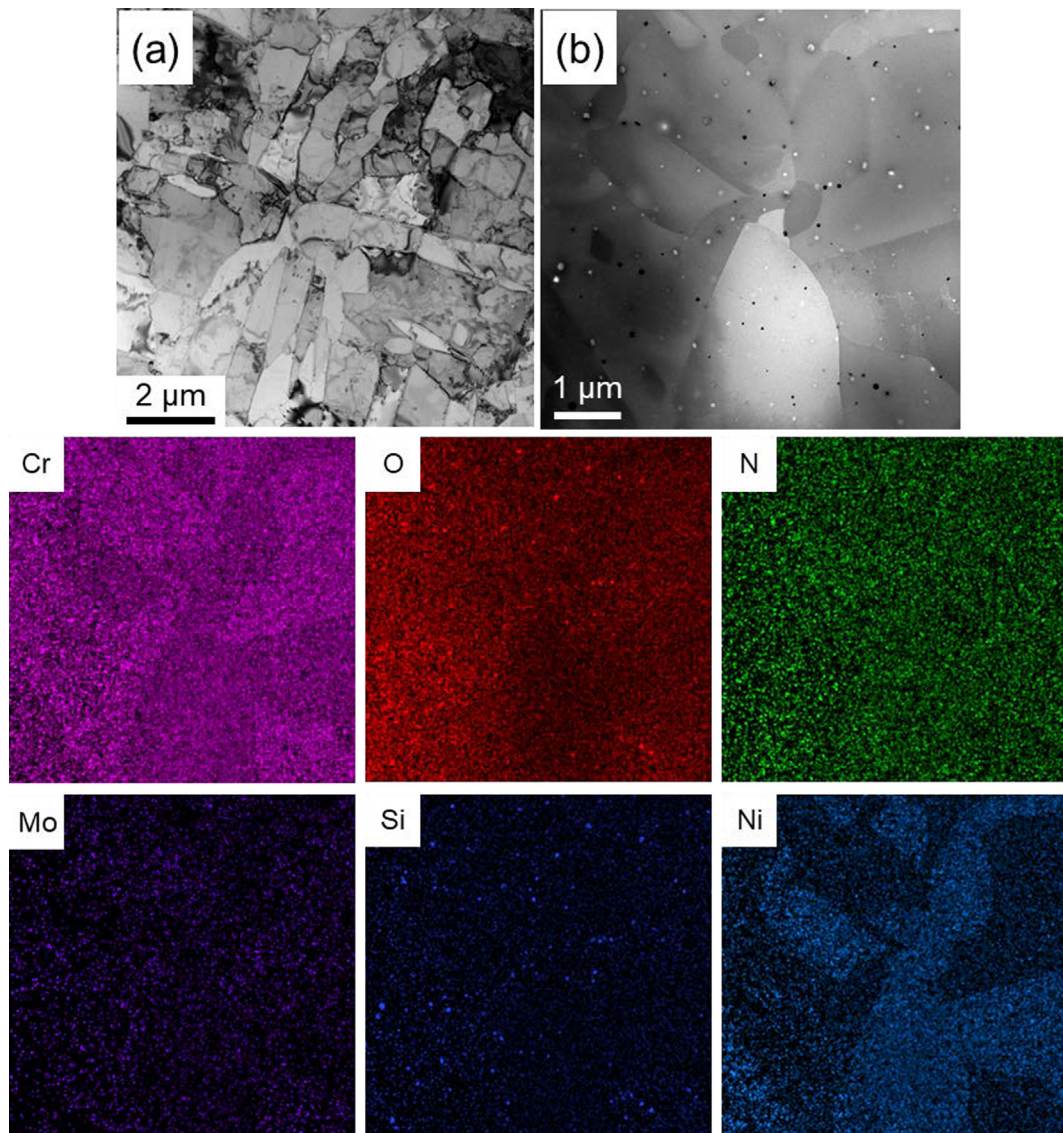


Fig. 4. (a) Bright-field TEM images showing austenite and ferrite grains within the heat-treated LPBF sample. (b) LAADF-STEM image of the microstructure with the corresponding elemental segregation in different phases.

remains above it for a few seconds is considered as CPT. CPT was measured to be 61 ± 1 °C for the hot-rolled specimen, which is in agreement with the literature for conventional 2205 DSS [44,45]. CPT decreased from 61 ± 1 °C for the hot-rolled specimen to 47 ± 2 °C for the as-built LPBF specimen, indicating a degradation in pitting corrosion resistance. This is an indication that the ferritic structure with numerous Cr₂N precipitates in the as-built LPBF material is less resistant to pitting corrosion at higher temperatures. Such phenomenon has been commonly reported for the welded joints in DSSs [46] and annealed DSSs at high temperatures [47]. The heat-treated LPBF specimen showed an enhanced CPT value of 61 ± 1 °C, which is similar to that of the hot-rolled specimen, suggesting the beneficial effects of short-time post-AM heat treatments in homogenising the microstructure and restoring the pitting corrosion resistance.

A comparison of the results obtained from polarisation measurements at room temperature to the CPT measurements indicates the significant importance of exposure temperature on the pitting susceptibility in LPBF 2205 DSS. With respect to corrosion resistance, the ratio of austenite to ferrite phases plays a crucial role as the partitioning of corrosion-resistant elements (e.g., Cr,

Mo, and N) favours the galvanic corrosion between those phases and consequently affects the corrosion resistance of DSSs [48,49]. Such elemental distribution is strongly dependent on the manufacturing route and post-manufacturing thermal processing. This phenomenon has been extensively investigated for conventionally manufactured DSSs based on the criterion called pitting resistance equivalent number (PREN). It is believed that a phase with a lower PREN value determines the pitting susceptibility [26]. In this regard, different grades of DSSs with various ratios of ferrite to austenite have been investigated in the literature. It has been generally reported that the pitting corrosion resistance decreases with increasing the ferrite content in the alloy [50–52].

The PREN for ferrite and austenite phases in DSSs is calculated based on Eq. (1), revealing the strong dependence of pitting resistance on the content of major alloying elements of Cr, Mo, and N.

$$\text{PREN} = \text{wt\%Cr} + 3.3 \times \text{wt\%Mo} + 16 \times \text{wt\%N} \quad (1)$$

In order to achieve better pitting corrosion resistance, both the austenite and ferrite phases must have PREN values that are high and close to each other. The concentration of alloying elements in ferrite and austenite phases determined by APT for the as-built

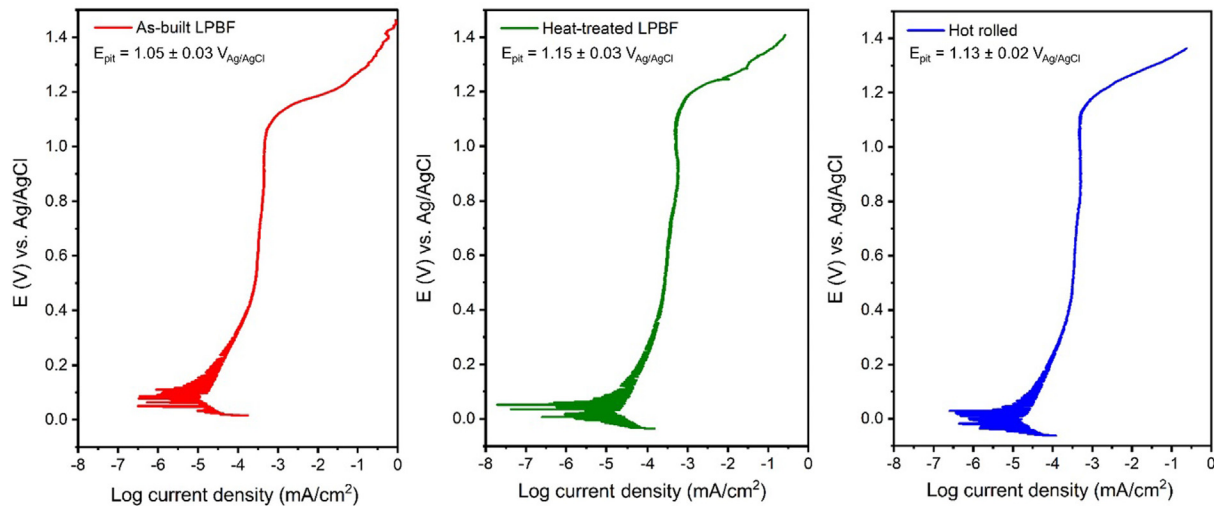


Fig. 5. Potentiodynamic polarisation curves for the as-built and heat-treated LPBF, and hot-rolled DSS specimens recorded in 1.0 M NaCl solution at room temperature (22 ± 2 °C). The average values for pitting potentials along with their standard deviations measured from at least five identical experiments for each specimen are also included in insets.

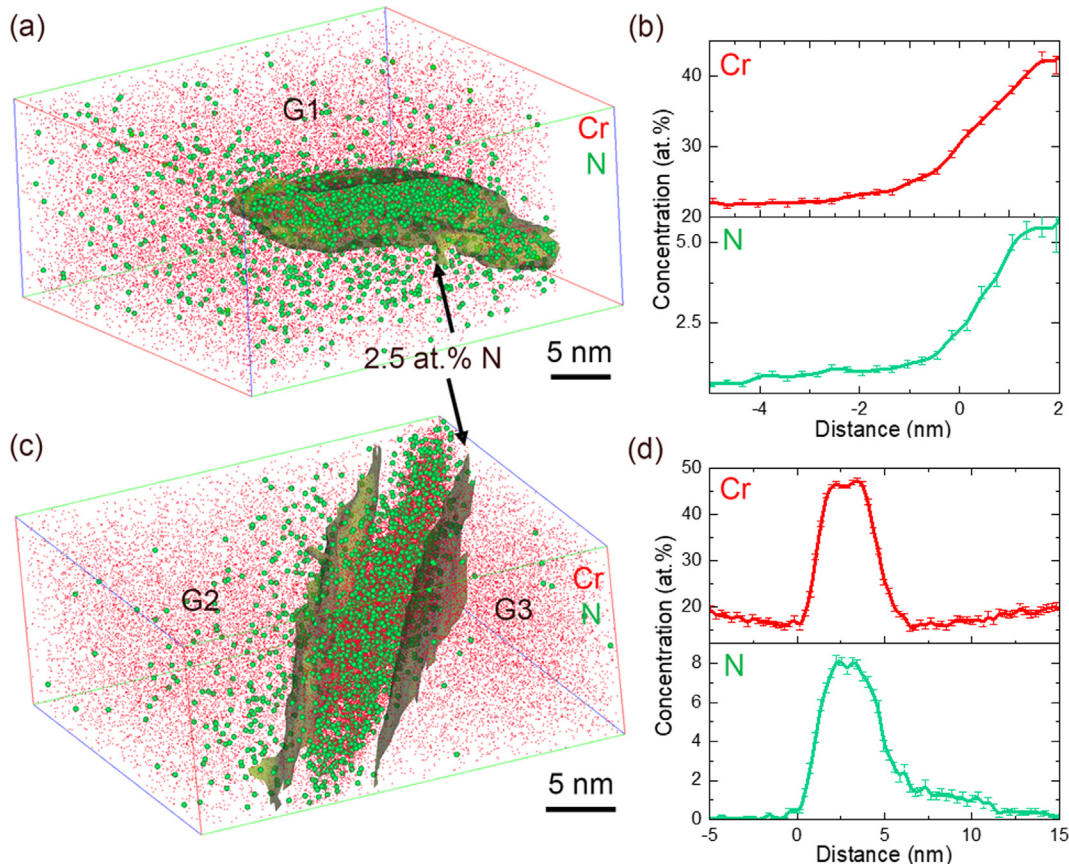


Fig. 6. (a) 3D atom distribution maps of Cr and N in a ferrite grain containing an intragranular CrN-rich phase. (b) Proxigram based on the 2.5 at.% N iso-concentration surfaces in (a). (c) 3D atom distribution maps of Cr and N across intergranular Cr-N rich grain boundary phase. (d) Proxigram based on the 2.5 at.% N iso-concentration surface in (c). G1, G2 and G3 indicate individual ferrite grains.

and heat-treated LPBF specimens are given in Table 2. The PREN values for austenite and ferrite phases are also calculated based on Eq. (1) and listed in Table 2. The PREN values for ferrite and austenite phases in the as-built LPBF specimen are 28.38 and 41.08, respectively. The low PREN of the ferrite phase could be due to the fact that the as-built LPBF specimen is almost fully ferritic, and the

ferrite-forming elements (i.e., Cr and Mo) are distributed over larger volumes of the ferrite phase, resulting in an overall decreased concentration of Cr and Mo in ferrite. This suggests a higher susceptibility of the ferrite phase to dissolution compared to the austenite phase at temperatures above CPT. The PREN values change after the post-AM heat treatment. The PREN for austenite decreases

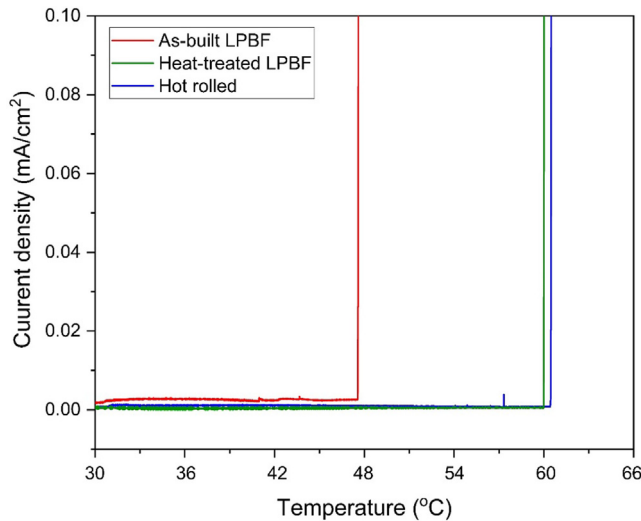


Fig. 7. Current changes versus temperature for different DSS specimens recorded in 1.0 M NaCl solution. The temperature at which the current density reached and remained above 0.1 mA/cm² is reported as the CPT.

(from 41.08 to 34.37) while that for ferrite increases (from 28.38 to 38.45). The PREN values for the heat-treated LPBF specimen are similar to those of the conventional 2205 DSS reported in the literature (generally in the range of 33–38 for both ferrite and austenite [49,53,54]). This further explains the similarity between the CPTs of hot-rolled and heat-treated LPBF specimens.

The surface morphologies of the corroded specimens after CPT experiments are presented in Fig. 8, indicating examples of corrosion pits. Fig. 8a shows that the ferrite phase was dissolved at temperatures above CPT, while Fig. 8b,c shows that pitting tends to start at the ferrite/austenite interface and then propagates towards austenite. This agrees with the chemical compositional difference between these two phases in DSSs, where the corrosion-resistant elements (e.g., Cr and Mo) are concentrated in ferrite (see STEM/EDS analysis in Fig. 4b).

Table 2

Chemical composition (wt%) and PREN for ferrite and austenite phases in as-built LPBF and heat-treated LPBF 2205 DSSs, determined by APM.

Specimen	Phase	Fraction	Cr	Ni	Mo	N	PREN
As-built LPBF	Ferrite	0.98	17.67	6.33	3.10	0.03	28.38
	Austenite	0.02	22.19	6.75	3.25	0.51	41.08
Heat-treated LPBF	Ferrite	0.55	23.72	3.95	4.27	0.04	38.45
	Austenite	0.45	19.99	7.57	2.71	0.34	34.37

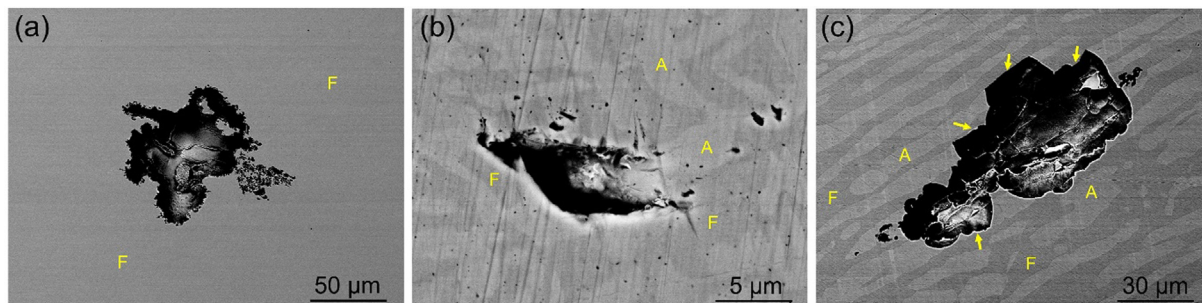


Fig. 8. Backscattered SEM images of typical corrosion pits on corroded surfaces of (a) as-built LPBF, (b) heat-treated LPBF, and (c) hot-rolled 2205 DSS after CPT experiments in 1.0 M NaCl solution. Regions with bright and grey contrasts in (b) and (c) indicate austenite and ferrite phases, respectively. These have also been marked with A and F for austenite and ferrite, respectively. Arrows in c show the austenite/ferrite interface, where the pitting seems to be started and propagated towards the austenite phase. Note that the scale bars in images for different samples are different.

- despite significant differences in their microstructures in terms of phase composition, precipitation behaviour, and elemental distribution.
- 3- Atom probe tomography reveals that no depletion of Cr occurs around intragranular Cr₂N in LPBF DSS. A deduction in Cr is observed adjacent to intergranular Cr₂N particles, however, Cr content in these regions remains above the critical value of 13 wt%.
 - 4- The as-built LPBF 2205 DSS shows a lower critical pitting temperature (CPT) compared to its hot-rolled counterpart (47 °C vs. 61 °C), while post-AM heat treatment results in an enhanced CPT comparable to the hot-rolled specimen (60 °C vs. 61 °C).
 - 5- The significantly lower PREN value for the ferrite phase in the as-built LPBF specimen is identified as the main reason for the low CPT for this specimen, which results in the preferential dissolution of the ferrite phase at temperatures above CPT. Post-AM heat treatment is able to almost equalize the PREN values for austenite and ferrite phases (to values similar to those in the conventional material), and thus enhance the CPT to values comparable to that of the hot-rolled sample.

Data availability statement

The raw/processed data required to reproduce these findings cannot be shared at this time as the data also forms part of an ongoing study.

CRediT authorship contribution statement

Nima Haghdadi: Methodology, Conceptualization, Formal analysis, Investigation, Data curation, Writing – original draft, Writing – review & editing. **Majid Laleh:** Methodology, Formal analysis, Investigation, Data curation, Writing – original draft, Writing – review & editing. **Hansheng Chen:** Formal analysis, Data curation, Writing – review & editing. **Zibin Chen:** Formal analysis, Data curation, Writing – review & editing. **Carina Ledermüller:** Formal analysis, Data curation, Writing – review & editing. **Xiaozhou Liao:** Conceptualization, Writing – review & editing, Funding acquisition. **Simon Ringer:** Conceptualization, Writing – review & editing, Funding acquisition. **Sophie Primig:** Methodology, Conceptualization, Writing – review & editing, Funding acquisition, Supervision.

Declaration of Competing Interest

The authors declare that they have no known competing financial interests or personal relationships that could have appeared to influence the work reported in this paper.

Acknowledgements

Funding from the AUSMURI program administered by the Australia's Department of Industry, Science, Energy and Resources is acknowledged. The authors acknowledge the facilities, as well as the scientific and technical support of the Electron Microscope Unit (EMU) at UNSW Sydney (part of the Mark Wainwright Centre) and Sydney Microscopy & Microanalysis (SMM) at the University of Sydney (a core research facility). Both the EMU and SMM are nodes of Microscopy Australia. The authors thank Dr. Xiaopeng Li and Mr. Qian Liu at UNSW Sydney for their kind help with 3D printing of materials. SP is supported under the Australian Research Council's DECRA (project number DE180100440) and the UNSW Scientia Fellowship schemes.

References

- [1] I. Gibson, D. Rosen, B. Stucker, M. Khorasani (Eds.), Additive Manufacturing Technologies, Third Ed., Springer International Publishing, New York, 2020.
- [2] T. DebRoy, H.L. Wei, J.S. Zuback, T. Mukherjee, J.W. Elmer, J.O. Milewski, A.M. Beese, A. Wilson-Heid, A. De, W. Zhang, Additive manufacturing of metallic components-process, structure and properties, *Prog. Mater Sci.* 92 (2018) 112–224.
- [3] N. Haghdadi, M. Laleh, M. Moyle, S. Primig, Additive manufacturing of steels: a review of achievements and challenges, *J. Mater. Sci.* 56 (2021) 64–107.
- [4] Y.M. Wang, T. Voisin, J.T. McKeown, J. Ye, N.P. Calta, Z. Li, Z. Zeng, Y. Zhang, W. Chen, T.T. Roehling, R.T. Ott, M.K. Santala, P. Depond, M.J. Matthews, A.V. Hamza, T. Zhu, Additively manufactured hierarchical stainless steels with high strength and ductility, *Nat. Mater.* 17 (1) (2018) 63–71.
- [5] Z. Sun, X. Tan, S.B. Tor, C.K. Chua, Simultaneously enhanced strength and ductility for 3D-printed stainless steel 316L by selective laser melting, *NPG Asia Mater.* 10 (4) (2018) 127–136.
- [6] Z.G. Zhu, Q.B. Nguyen, F.L. Ng, X.H. An, X.Z. Liao, P.K. Liaw, S.M.L. Nai, J. Wei, Hierarchical microstructure and strengthening mechanisms of a CoCrFeNiMn high entropy alloy additively manufactured by selective laser melting, *Scripta Mater.* 154 (2018) 20–24.
- [7] M. Laleh, A.E. Hughes, W. Xu, N. Haghdadi, K. Wang, P. Cizek, I. Gibson, M.Y. Tan, On the unusual intergranular corrosion resistance of 316L stainless steel additively manufactured by selective laser melting, *Corros. Sci.* 161 (2019) 108189.
- [8] Q.i. Chao, V. Cruz, S. Thomas, N. Birbilis, P. Collins, A. Taylor, P.D. Hodgson, D. Fabijanic, On the enhanced corrosion resistance of a selective laser melted austenitic stainless steel, *Scripta Mater.* 141 (2017) 94–98.
- [9] M. Laleh, A.E. Hughes, S. Yang, J. Li, W. Xu, I. Gibson, M.Y. Tan, Two and three-dimensional characterisation of localised corrosion affected by lack-of-fusion pores in 316L stainless steel produced by selective laser melting, *Corros. Sci.* 165 (2020) 108394.
- [10] T. Niendorf, S. Leuders, A. Riemer, H.A. Richard, T. Tröster, D. Schwarze, Highly anisotropic steel processed by selective laser melting, *Metall. Mater. Trans. B* 44 (4) (2013) 794–796.
- [11] H. Wang, Z.G. Zhu, H. Chen, A.G. Wang, J.Q. Liu, H.W. Liu, R.K. Zheng, S.M.L. Nai, S. Primig, S.S. Babu, S.P. Ringer, X.Z. Liao, Effect of cyclic rapid thermal loadings on the microstructural evolution of a CrMnFeCoNi high-entropy alloy manufactured by selective laser melting, *Acta Mater.* 196 (2020) 609–625.
- [12] M. Laleh, A.E. Hughes, M.Y. Tan, G.S. Rohrer, S. Primig, N. Haghdadi, Grain boundary character distribution in an additively manufactured austenitic stainless steel, *Scripta Mater.* 192 (2021) 115–119.
- [13] K. Saeidi, X. Gao, Y. Zhong, Z.J. Shen, Hardened austenite steel with columnar sub-grain structure formed by laser melting, *Mater. Sci. Eng., A* 625 (2015) 221–229.
- [14] F. Yan, W. Xiong, E. Faierson, G.B. Olson, Characterization of nano-scale oxides in austenitic stainless steel processed by powder bed fusion, *Scripta Mater.* 155 (2018) 104–108.
- [15] K. Saeidi, L. Kvetková, F. Lofaj, Z. Shen, Austenitic stainless steel strengthened by the in situ formation of oxide nanoinclusions, *RSC Adv.* 5 (27) (2015) 20747–20750.
- [16] K.H. Lo, C.H. Shek, J. Lai, Recent developments in stainless steels, *Mater. Sci. Eng.: R: Rep.* 65 (4–6) (2009) 39–104.
- [17] M. Laleh, A.E. Hughes, W. Xu, I. Gibson, M.Y. Tan, A critical review of corrosion characteristics of additively manufactured stainless steels, *Int. Mater. Rev.* 66 (8) (2021) 563–599.
- [18] P. Bajaj, A. Hariharan, A. Kini, P. Kürnsteiner, D. Raabe, E.A. Jägle, Steels in additive manufacturing: A review of their microstructure and properties, *Mater. Sci. Eng., A* 772 (2020) 138633, <https://doi.org/10.1016/j.msea.2019.138633>.
- [19] M. Laleh, A.E. Hughes, W. Xu, I. Gibson, M.Y. Tan, A critical review of corrosion characteristics of additively manufactured stainless steels, *Int. Mater. Rev.* 1–37 (2020).
- [20] K. Davidson, S. Singamneni, Selective laser melting of duplex stainless steel powders: an investigation, *Mater. Manuf. Processes* 31 (12) (2016) 1543–1555.
- [21] F. Hengsbach, P. Koppa, K. Duschik, M.J. Holzweissig, M. Burns, J. Nellesen, W. Tillmann, T. Tröster, K.-P. Hoyer, M. Schaper, Duplex stainless steel fabricated by selective laser melting-Microstructural and mechanical properties, *Mater. Des.* 133 (2017) 136–142.
- [22] K. Saeidi, L. Kvetková, F. Lofaj, Z. Shen, Novel ferritic stainless steel formed by laser melting from duplex stainless steel powder with advanced mechanical properties and high ductility, *Mater. Sci. Eng., A* 665 (2016) 59–65.
- [23] G.N. Nigon, O.B. Isgor, S. Pasebani, The effect of annealing on the selective laser melting of 2205 duplex stainless steel: Microstructure, grain orientation, and manufacturing challenges, *Opt. Laser Technol.* 134 (2021) 106643.
- [24] S. Papula, M. Song, A. Pateras, X.-B. Chen, M. Brandt, M. Easton, Y. Yagodzinsky, I. Virkkunen, H. Hänninen, Selective laser melting of duplex stainless Steel 2205: Effect of post-processing heat treatment on microstructure, mechanical properties, and corrosion resistance, *Materials* 12 (15) (2019) 2468.

- [25] N. Haghadi, M. Laleh, A. Kosari, M.H. Moayed, P. Cizek, P.D. Hodgson, H. Beladi, The effect of phase transformation route on the intergranular corrosion susceptibility of 2205 duplex stainless steel, *Mater. Lett.* 238 (2019) 26–30.
- [26] H. Tan, Y. Jiang, B.O. Deng, T. Sun, J. Xu, J. Li, Effect of annealing temperature on the pitting corrosion resistance of super duplex stainless steel UNS S32750, *Mater. Charact.* 60 (9) (2009) 1049–1054.
- [27] L.F. Garfias-Mesias, J.M. Sykes, C.D.S. Tuck, The effect of phase compositions on the pitting corrosion of 25 Cr duplex stainless steel in chloride solutions, *Corros. Sci.* 38 (8) (1996) 1319–1330.
- [28] P. Murkute, S. Pasebani, O.B. Isgor, Effects of heat treatment and applied stresses on the corrosion performance of additively manufactured super duplex stainless steel clads, *Materialia* 14 (2020) 100878.
- [29] D. Jiang, N. Birbilis, C. Hutchinson, M. Brameld, On the microstructure and electrochemical properties of additively manufactured duplex stainless steels produced using laser-powder bed fusion, *Corrosion* 76 (9) (2020) 871–883.
- [30] R.J. BRIGHAM, E.W. TOZER, Temperature as a pitting criterion, *Corrosion* 29 (1) (1973) 33–36.
- [31] V.M. Salinas-Bravo, R.C. Newman, An alternative method to determine critical pitting temperature of stainless steels in ferric chloride solution, *Corros. Sci.* 36 (1) (1994) 67–77.
- [32] N. Haghadi, P. Cizek, H. Beladi, P.D. Hodgson, A novel high-strain-rate ferrite dynamic softening mechanism facilitated by the interphase in the austenite/ferrite microstructure, *Acta Mater.* 126 (2017) 44–57.
- [33] M.K. Miller, K.F. Russell, G.B. Thompson, Strategies for fabricating atom probe specimens with a dual beam FIB, *Ultramicroscopy* 102 (4) (2005) 287–298.
- [34] B. Gault, M.P. Moody, J.M. Cairney, S.P. Ringer, *Atom probe microscopy*, Springer Science & Business Media, 2012.
- [35] A. Rokanopoulou, G.D. Papadimitriou, Production of high nitrogen surfaces on 2205 duplex stainless steel substrate using the PTA technique, *Mater. Sci. Technol.* 27 (9) (2011) 1391–1398.
- [36] N. Haghadi, P. Cizek, P.D. Hodgson, V. Tari, G.S. Rohrer, H. Beladi, Effect of ferrite-to-austenite phase transformation path on the interface crystallographic character distributions in a duplex stainless steel, *Acta Mater.* 145 (2018) 196–209.
- [37] N. Haghadi, P. Cizek, P. Hodgson, H. Beladi, Microstructure dependence of impact toughness in duplex stainless steels, *Mater. Sci. Eng., A* 745 (2019) 369–378.
- [38] N. Haghadi, P. Cizek, P.D. Hodgson, Y. He, B. Sun, J.J. Jonas, G.S. Rohrer, H. Beladi, New insights into the interface characteristics of a duplex stainless steel subjected to accelerated ferrite-to-austenite transformation, *J. Mater. Sci.* 55 (12) (2020) 5322–5339.
- [39] V.A. Hosseini, S. Wessman, K. Hurtig, L. Karlsson, Nitrogen loss and effects on microstructure in multipass TIG welding of a super duplex stainless steel, *Mater. Des.* 98 (2016) 88–97.
- [40] Y. Zhao, Y. Sun, X. Li, F. Song, In-situ observation of $\delta \leftrightarrow \gamma$ phase transformations in duplex stainless steel containing different nitrogen contents, *ISIJ Int.* (2017). ISIJINT-2017-125.
- [41] D. Kotecki, T. Siewert, WRC-1992 constitution diagram for stainless steel weld metals: a modification of the WRC-1988 diagram, *Welding J.* 71 (5) (1992) 171–178.
- [42] E. Bettini, U. Kivisäkk, C. Leygraf, J. Pan, Study of corrosion behavior of a 22% Cr duplex stainless steel: Influence of nano-sized chromium nitrides and exposure temperature, *Electrochim. Acta* 113 (2013) 280–289.
- [43] G. Frankel, Pitting corrosion of metals: a review of the critical factors, *J. Electrochem. Soc.* 145 (6) (1998) 2186–2198.
- [44] N. Ebrahimi, M. Momeni, A. Kosari, M.H. Moayed, A comparative study of critical pitting temperature (CPT) of stainless steels by electrochemical impedance spectroscopy (EIS), potentiodynamic and potentiostatic techniques, *Corros. Sci.* 59 (2012) 96–102.
- [45] B.O. Deng, Y. Jiang, J. Gong, C. Zhong, J. Gao, J. Li, Critical pitting and repassivation temperatures for duplex stainless steel in chloride solutions, *Electrochim. Acta* 53 (16) (2008) 5220–5225.
- [46] Y. Yang, Z. Wang, H. Tan, J. Hong, Y. Jiang, L. Jiang, J. Li, Effect of a brief post-weld heat treatment on the microstructure evolution and pitting corrosion of laser beam welded UNS S31803 duplex stainless steel, *Corros. Sci.* 65 (2012) 472–480.
- [47] M. Naghizadeh, M.H. Moayed, Investigation of the effect of solution annealing temperature on critical pitting temperature of 2205 duplex stainless steel by measuring pit solution chemistry, *Corros. Sci.* 94 (2015) 179–189.
- [48] H.-Y. Ha, T.-H. Lee, C.-G. Lee, H. Yoon, Understanding the relation between pitting corrosion resistance and phase fraction of S32101 duplex stainless steel, *Corros. Sci.* 149 (2019) 226–235.
- [49] H.-Y. Ha, M.-H. Jang, T.-H. Lee, J. Moon, Interpretation of the relation between ferrite fraction and pitting corrosion resistance of commercial 2205 duplex stainless steel, *Corros. Sci.* 89 (2014) 154–162.
- [50] Z. Zhang, Z. Wang, Y. Jiang, H. Tan, D. Han, Y. Guo, J. Li, Effect of post-weld heat treatment on microstructure evolution and pitting corrosion behavior of UNS S31803 duplex stainless steel welds, *Corros. Sci.* 62 (2012) 42–50.
- [51] Y. Yang, H. Tan, Z. Zhang, Z. Wang, Y. Jiang, L. Jiang, J. Li, Effect of annealing temperature on the pitting corrosion behavior of UNS S82441 duplex stainless steel, *Corrosion* 69 (2) (2013) 167–173.
- [52] M. Gholami, M. Hoseinpoor, M.H. Moayed, A statistical study on the effect of annealing temperature on pitting corrosion resistance of 2205 duplex stainless steel, *Corros. Sci.* 94 (2015) 156–164.
- [53] Z. Zhang, H. Jing, L. Xu, Y. Han, L. Zhao, X. Lv, Effect of post-weld heat treatment on microstructure evolution and pitting corrosion resistance of electron beam-welded duplex stainless steel, *Corros. Sci.* 141 (2018) 30–45.
- [54] Z. Zhang, H. Jing, L. Xu, Y. Han, L. Zhao, The influence of microstructural evolution on selective corrosion in duplex stainless steel flux-cored arc welded joints, *Corros. Sci.* 120 (2017) 194–210.
- [55] M. Laleh, A.E. Hughes, W. Xu, P. Cizek, M.Y. Tan, Unanticipated drastic decline in pitting corrosion resistance of additively manufactured 316L stainless steel after high-temperature post-processing, *Corros. Sci.* 165 (2020) 108412.
- [56] A. Barroux, N. Ducommun, E. Nivet, L. Laffont, C. Blanc, Pitting corrosion of 17-4PH stainless steel manufactured by laser beam melting, *Corros. Sci.* 169 (2020) 108594.
- [57] D. Kong, C. Dong, X. Ni, L. Zhang, H. Luo, R. Li, L. Wang, C. Man, X. Li, The passivity of selective laser melted 316L stainless steel, *Appl. Surf. Sci.* 504 (2020) 144495.